JGR Space Physics

RESEARCH ARTICLE
10.1029/2023JA032364

Secondary Gravity Wave Propagation in Tropical Thermospheric Region: Role of Varying Kinematic Viscosity

Soumen Datta[1], **Saurabh Das**[1], **and Surendra Sunda**[2]

[1]Department of Astronomy, Astrophysics and Space Engineering, IIT Indore, Indore, Madhya Pradesh, India, [2]Airport Authority of India, Ahmedabad, Gujarat, India

Key Points:

- The study presents signature of thunderstorm induced gravity wave above lower thermospheric altitude
- Phase velocity and intrinsic period increased linearly from thunderstorm location
- An almost unique wave dissipation altitude found for all waves for a specific kinematic viscosity

Correspondence to:

S. Das,
das.saurabh01@gmail.com

Citation:

Datta, S., Das, S., & Sunda, S. (2024). Secondary gravity wave propagation in tropical thermospheric region: Role of varying kinematic viscosity. *Journal of Geophysical Research: Space Physics*, *129*, e2023JA032364. https://doi.org/10.1029/2023JA032364

Received 11 DEC 2023
Accepted 2 OCT 2024

Author Contributions:

Conceptualization: Soumen Datta
Data curation: Surendra Sunda
Formal analysis: Saurabh Das, Surendra Sunda
Funding acquisition: Saurabh Das
Investigation: Soumen Datta, Saurabh Das
Methodology: Soumen Datta, Saurabh Das, Surendra Sunda
Resources: Soumen Datta, Saurabh Das, Surendra Sunda
Software: Soumen Datta
Supervision: Saurabh Das, Surendra Sunda
Validation: Soumen Datta
Writing – original draft: Soumen Datta
Writing – review & editing: Saurabh Das, Surendra Sunda

Abstract The current study has investigated the thunderstorm induced atmospheric gravity waves (AGWs) over Indian region based on the perturbation signatures in ionospheric total electron content (TEC) measurement. Robust traveling ionospheric disturbance (TID) signature has been identified along the east side of the thunderstorm affected area. Neutral wind was found to have a favorable impact in this aspect for a certain time duration of the day by modulating the vertical wavelength. The role of temperature was analyzed in terms of kinematic viscosity which is a crucial component, especially over tropical region, for wave dissipation and reflection along its propagation path. Ray tracing algorithm is also applied with varying kinematic viscosity and thermal diffusivity for retrieval of possible ray paths and source location of observed waves. A statistical investigation has been carried out to identify the dissipation altitude of observed waves along the ray paths. It has been found that all waves dissipated at almost a constant altitude for a specific kinematic viscosity and above this altitude vertical wavelength was found to decrease. The ray paths interacted at a common point which was located at about 125 km altitude and was very close to the region of maximum lightning activity. It can also be noted that the observed phase velocities can't be achieved by a wave below the turbopause. It indicates that the observed waves were excited from a secondary source and not directly connected to convective system. The study provides an in-depth analysis of mesoscale system induced gravity wave propagation and dissipation over tropical region.

Plain Language Summary Mesoscale convective systems in tropical regions are key sources of low-frequency atmospheric gravity waves (GWs). GWs usually generates above thunderstorm altitudes and propagates to ionospheric heights through dissipation and atmospheric filtering. This is one of the first study about the propagation mechanism of thunderstorm-generated GWs at thermospheric altitude over the Indian region. The concentric source of the wave was evidenced by concentric rings in traveling ionospheric disturbance and phase velocity (V_p) trends which coincides with high lightning location. It is also observed that wave with V_p above 250 m/s were unable to propagate below 100 Km and indicate the secondary source of the gravity wave at thermospheric altitudes which was not directly related with the thunderstorm activity. The effect of background temperature on the propagation mechanism was tested by examining the role of kinematic viscosity on wave dissipation. The maximum momentum fluxes were found around 260 km altitude for a specific kinematic viscosity profile. Interestingly, the ray-tracing validation fails one scale height above this altitude, aligning with theories of wave dissipation or reflection. Additionally, it was also observed that all waves interacted at a common point in both horizontal and temporal domains. This is one of the key finding of this investigation.

1. Introduction

Last few decades have witnessed a surge in number of fundamental researches being carried out on the impact of various low frequency atmospheric waves and their roles on climatic patterns. Atmospheric gravity wave (AGW), which is one of the dominant ones among these low frequency waves, are primarily generated by atmospheric tidal oscillation, overshooting of convective systems(Lay et al., 2015; Vadas et al., 2009; Vadas & Fritts, 2004), wind shear force (Du et al., 2019; Hines, 1960; Y. Wang et al., 2019), orographic lifting forces (P. Alexander et al., 2015; Figueiredo et al., 2023; Vadas & Nicolls, 2009) etc. Along with the atmospheric filtering process, the transfer of energy and momentum from one region to another takes places which happens to be the actual mechanism behind gravity wave propagation (Fritts & Alexander, 2003). The mesosphere and lower thermosphere are responsible for dissipation of most of the waves by depositing their entire energy and momentum (Hickey & Coley, 1988; Richmond, 1978; Vadas & Fritts, 2005, 2006). The horizontal acceleration of the fluid by

averaging over one wavelength is influenced by the vertical divergence of the momentum flux of primary waves (Andrews et al., 1987). Along with the acceleration, an altered mean wind and corresponding residual circulation are excited by the deposition of momentum flux in the mesosphere and lower thermosphere region (Vadas et al., 2003). In few cases AGWs containing large vertical wavelength and phase speed are capable of avoiding the breaking process and reach ionosphere-thermosphere altitude and experience non-linear breaking mechanism (Heale et al., 2014; Vadas, 2007). However, a significantly large effect occurs in the mean circulation of the dissipation altitude due to the wave breaking process and produces secondary waves (Vadas et al., 2003; Vadas & Fritts, 2001). Secondary waves, generated by local body forces, can propagate in all directions except perpendicular to the force. The basic characteristics of the waves like intrinsic frequency and momentum flux, depend on the spatio-temporal features of the body force. These waves significantly perturb neutral atmospheric parameters like wind velocity, temperature, and density. Unlike primary GWs, secondary waves have a higher phase velocity of about 500–600 m/s, larger horizontal and vertical wavelengths, and a smaller intrinsic frequency (Vadas & Azeem, 2021; Vadas & Crowley, 2010).

The wave like signatures at thermospheric altitude were first evidenced by (Munro, 1948) and latter the presence of GW at this altitude was theoretically explained by the pioneer works of (Hines, 1960, 1974). Several investigations have been carried out on the propagation of GWs at thermospheric altitude using different instruments like airglow, ionosonde, incoherent scatter radar or with the help of total electron content (TEC) extracted from GPS signal. The interest on TEC based measurements has increased significantly in recent past due to its capability of continuous observation with low operational cost. The basic motivation behind these studies have been the investigation of wave properties from perturbed signatures, called traveling ionospheric disturbances (TID) (Azeem et al., 2017; Hernndez-Pajares et al., 2006; Hocke & Schlegel, 1996; Occhipinti et al., 2008). Several studies indicated that the convectively generated GWs have a common point source and it appear in the mesosphere or (M. J. Alexander, 1996; Horinouchi et al., 2002; Lane & Sharman, 2006) lower thermosphere (Azeem et al., 2015; Figueiredo et al., 2023; Nishioka et al., 2013; Vadas et al., 2009) with a conical shaped phase surface by altering its mean state in presence of zero or small background wind. These TIDs associated with GWs exhibit large horizontal wavelengths and high phase velocities due to their rapid increase in vertical wavelength and phase velocity at thermospheric altitude which starts from approximately 110 km extends to nearly 600 km altitude. This region, characterized by low density and high temperature, significantly affects kinematic viscosity and thermal diffusivity, which are crucial for wave propagation. Previous studies have explored the theoretical mechanisms of wave propagation with kinematic viscosity (Vadas & Fritts, 2005) and its impact on wave behavior under varying solar conditions (Cole & Hickey, 1981; Pitteway & Hines, 1963; Richmond, 1978; Vadas & Fritts, 2006). Our investigation further examines the role of kinematic viscosity in wave dissipation in the tropical region, using model temperature data.

This study is focusing on the ionospheric TEC perturbations from GPS signals after a severe thunderstorm, investigating on traveling ionospheric disturbance (TID) signatures to analyze GWs induced by convective systems in tropical regions. By using ray tracing with kinematic viscosity and thermal diffusivity, the study identifies a unique dissipation altitude for a specific kinematic viscosity in zero background wind. The results align with the observed vertical wavelengths and show that horizontal ray paths intersect near locations of high lightning activity. This suggests that kinematic viscosity plays a significant role in wave propagation in the tropical belt. The study location, observations and methodology of TID measurement from GPS data are mentioned in Section 2. The signature of TIDs and theoretical representation of concentric GW and ray-tracing algorithm is mentioned in Section 3. The result analysis has been done in Section 4. The statistical investigation on effective kinematic viscosity for the observed waves have been discussed in this section. And finally the probable ray paths extraction in different wind condition is mentioned.

2. Location, Data and Methodology

2.1. Study Location

The study location Kolkata (22.65°N and 88.37°E) is a tropical location and quite suitable for studying convective systems and its consequences due to the vicinity of ITCZ line. The land-sea temperature difference in this area is very high which influences various convective activities like lightning especially during the pre-monsoon (Tinmaker & Chate, 2013). The area is extremely prone to various types of cyclonic movements, mesoscale developments, squall line events and Norwesters.

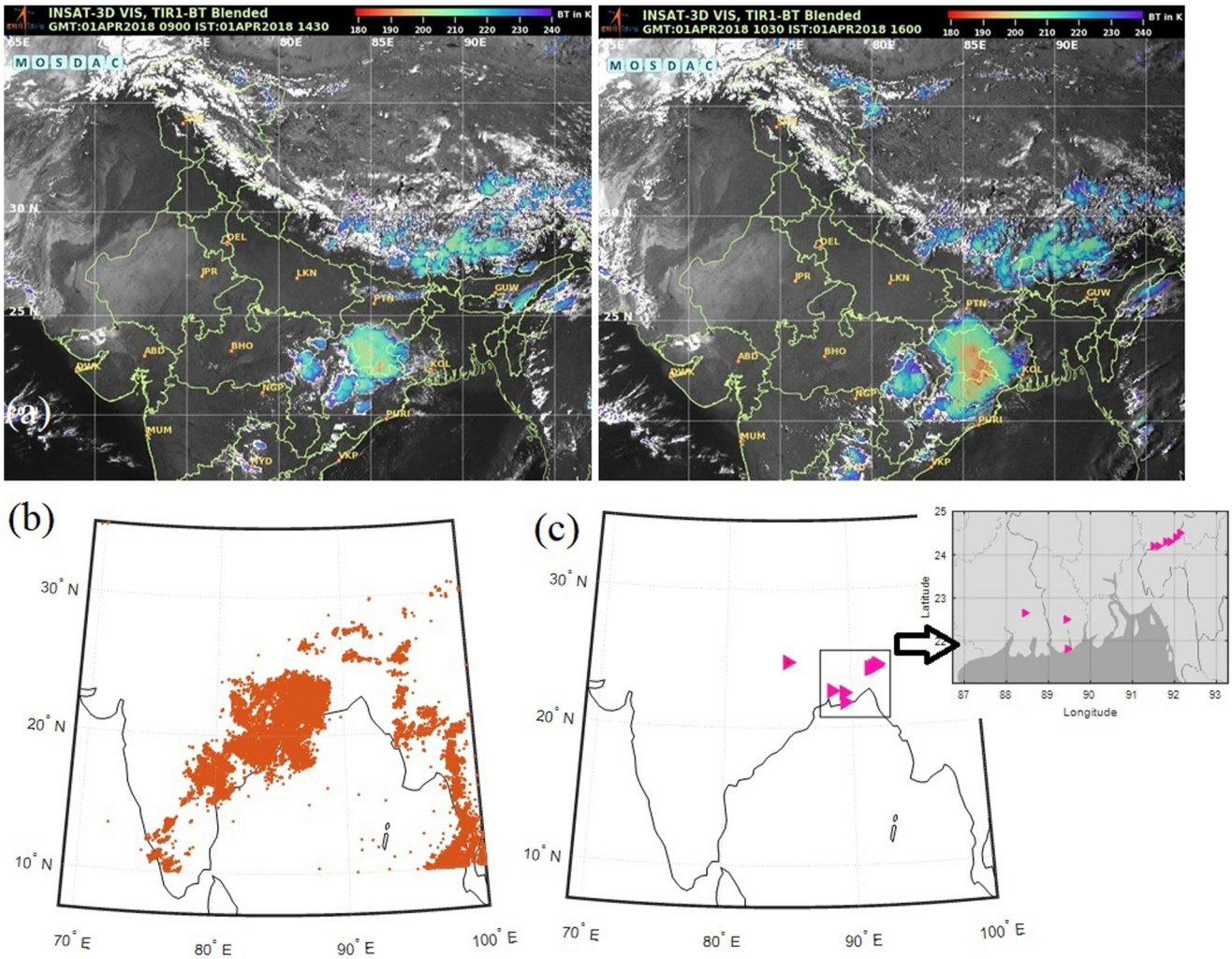

Figure 1. (a) Cloud system signatures during two different time obtained from INSAT-3DR Imager retrieved brightness temperature; (b) Lightning strike locations over the study area; (c) Position of GPS receivers used for this study.

2.2. Data Sources

A convective system developed on 1 April 2018 has been studied. The event caused severe thunderstorm and significant number of lightning strikes over a wide part of both the coastal and inner-landmass areas of the Eastern India. The convective system information is obtained from INSAT-3D satellite imagery [https://www.mosdac.gov.in]. INSAT is a series of satellites with geostationary constellation. Figure 1a shows the satellite images of the system at two different time instants (09:00 and 10:30 UTC). The convective system developed over the central India and gradually moved toward the eastern part. A significant number of lightning strikes also were observed over the said region (Figure 1b). Lightning strike information are obtained from WWLLN ground based lightning location network [http://wwlln.net/] with 70 stations around the globe. The development of thunderstorm system and occurrence of lightning strikes brings our interest to investigate the consequences at ionospheric altitude with the help of dual frequency GPS receivers installed at the several locations near the region (Figure 1c).

Navigation data has been collected from dual frequency GPS receivers from UNAVCO archive database [https://www.unavco.org/]. Here, the data from UNAVCO Bangladesh network consisting of several GPS receivers, which are installed closed to our study location, is used for this study. The data from two reference grade Dual-Frequency GPS receivers at Kolkata and Gaya operating under GAGAN—TEC Network is also used. GAGAN is an Indian Satellite Based Augmentation System (SBAS) which was jointly developed by Airport Authority of

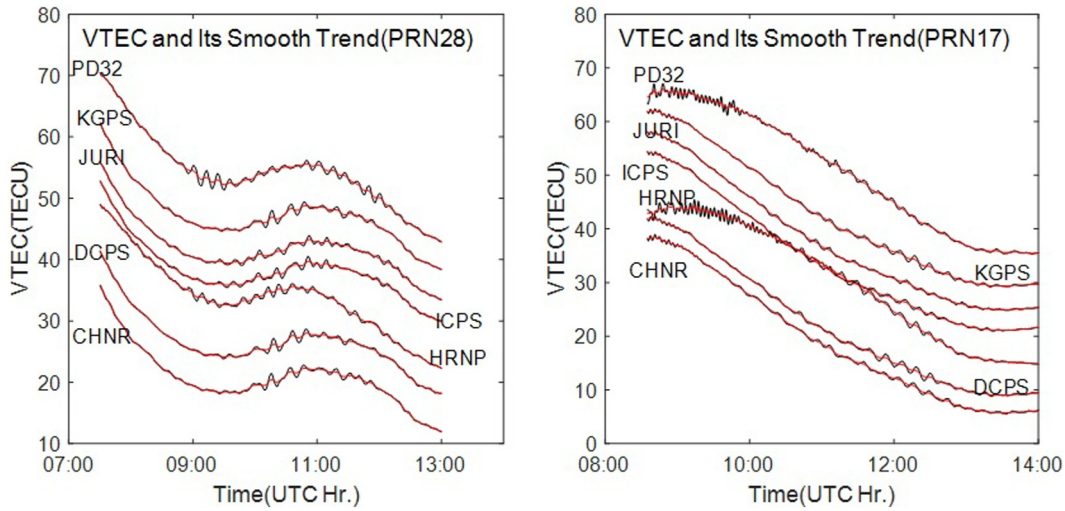

Figure 2. Carrier phase based VTEC measurement (black lines) and its soft trend (red lines) over the day.

India and ISRO for highly precise positioning service. The GAGAN TEC Network consisting of strategically located 25 stations was used for characterizing and developing the ionospheric model for Indian region.

2.3. Methodology

The TEC measurement with code carrier combination have a very less noise effect of 0.01–0.1 TECU (Burrell et al., 2009). The carrier phase delay based measurement of this TEC have a very soft trend in calm condition (Lay et al., 2013; Rahmani et al., 2020). Hence any ionospheric disturbance can be measured based on the sudden change on the TEC time series. The slant TEC (STEC) along the line of sight from receiver to the satellite can be computed by using two frequency carrier phase delay measurements:

$$TEC_{slant} = \frac{1}{40.3}\frac{f_1^2 * f_2^2}{f_1^2 - f_2^2}[L_1 - L_2 + \lambda_1 N_1 - \lambda_2 N_2 + b_{r-s}] \quad (1)$$

L_1 and L_2 are carrier phase delay measurements at frequency f_1 and f_2 respectively. N_1 and N_2 are ambiguities in carrier phase delay. b_{r-s} is the biasing combination between receiver and satellite. The biasing and ambiguity remain constant for almost 24 hr duration if no cycle slip occurs. Cycle slip correction is crucial part for estimation of ionospheric perturbation and can be done with the different combinations of dual frequency pseudorange and carrier phase delay measurement (Datta & Das, 2023). After removal of cycle slip STEC is converted to vertical TEC (VTEC) by elevation angle dependent mapping function by assuming that the ionospheric pierce points are located at 350 km altitude. The entire data processing can be found in Kaplan and Hagerty (2006). The carrier phase-based TEC measurement has both its actual variation and its smooth trend over the day. Hence, the perturbation in TEC measurement can be computed by removing its soft trend from the actual value. Here, this differential TEC (dTEC) calculation is carried out from the difference between the actual time series and 1 hr moving average value(±30min)(Figueiredo et al., 2023; Tsugawa et al., 2007). Figure 2 Shows the VTEC variation of two different satellites from seven different receivers. The black curves indicate the actual measurement, and the red lines indicate the smooth trend of respective VTEC measurement. Significant perturbation signatures were observed from VTEC measurement and its smoothed variation and it reached almost 0.6 TECU. Further the properties of waves have been estimated from the dTEC measurement and the detail of computation techniques have been included in *Results and Discussion* section.

3. Gravity Wave Propagation Mechanism and Ray Tracing

3.1. Traveling Ionospheric Disturbance Signature

Noteworthy TID signature was observed in several GPS satellite signals (Figure 3). Though ionospheric perturbations as identified previously, was caused by this thunderstorm induced acoustic-gravity wave (Datta &

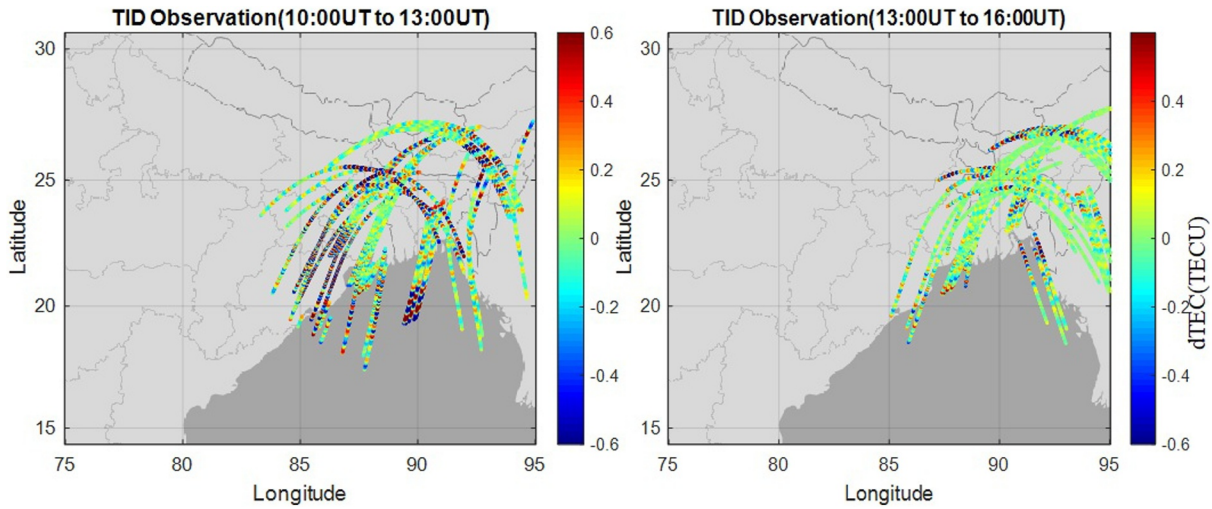

Figure 3. TID signatures identified at IPP location of several GPS satellites during two different time duration. The left side one indicates the signatures during 10:00 to 13:00 UTC and the right side figure shows the signature during 13:00 to 16:00 UTC.

Das, 2023), here our focus is on the propagation of GW only. No geomagnetic disturbances were noted during the observation day and its consecutive days which indicates that the deep convection might be a possible reason behind the ionospheric perturbation. The temporal change of the perturbation signature is highly indicative. No significant signatures were found before 9:00 UTC which was very early stage of thunderstorm system development. But the disturbances started to become noteworthy after 9:00 UTC and the TID amplitudes gradually started increasing and reached up to its maximum of about 0.8TECU. Figure 3. Shows the IPP location of the satellites by which the TID signatures were detected separately during two different time duration. Instead of showing individual TID variation it is showed based on the IPP location and the colors indicate its amplitude. Strong perturbation signatures were detected by sufficient numbers of satellites during the initial phase (10:00 UTC to 13:00 UTC) of the perturbation. The signatures were smaller in the next phase of the observation (from 13:00 UTC to 15:00 UTC) which can be attributed by two possible reasons. Here, the time of the event was local post-sunset hours and also the associated atmospheric parameters such as wind flow was also not favorable for the GW to reach this high altitude in this direction.

3.2. Background Atmospheric Parameters

The TID signatures at the IPP location of GPS satellites showed that the TIDs along the east side of the thunderstorm affected area were more dominating during 10:00 to 13:00UT (Figure 3a) compared to the other observation periods. The background atmospheric conditions play crucial roles in GW propagation. The atmospheric parameters such as neutral density and temperature variation data has been collected from NRLMSISE-00 model (Picone et al., 2002). The horizontal wind shear measurement has been taken from empirical Horizontal Wind Model-14 (HWM-14). A strong westward and northwestward wind flow was observed during 10:00 UTC (Figure 4b) over the study location. An almost similar wind structure was observed 1 hour before and after this time. Hence, it is prevalent that westward propagating waves will face higher dissipative force compared to the eastward because of the smaller vertical wavelength. But during the next period of observation that is, after 13:00 UTC an almost opposite wind structure was observed (Figure 4c) and it opposed the wave to reach the ionospheric altitude.

Other two key parameters, kinematic viscosity (ν) and thermal diffusivity (κ), are also investigated to study the propagation process further. A rapid increase of atmospheric temperature from lower thermospheric altitude (~100 km) was observed and it becomes almost constant above 250 km altitude. Hence the molecular viscosity (μ) which can be expressed by Equation 16, becomes constant. It introduces a serious discrepancy in the AGW propagation model because of the rapid decrease in neutral density at this altitude. The molecular distance and mean free path variation with altitude is shown in Figures 4d and 4e. Both of this parameters showed significantly large values above 200 km altitude. Hence, it can't be constant μ with altitude. Besides, the constant μ generates a very rapid increase of kinematic viscosity (ν) which can be expressed as $\nu = \mu/\rho$; where ρ is neutral density. A

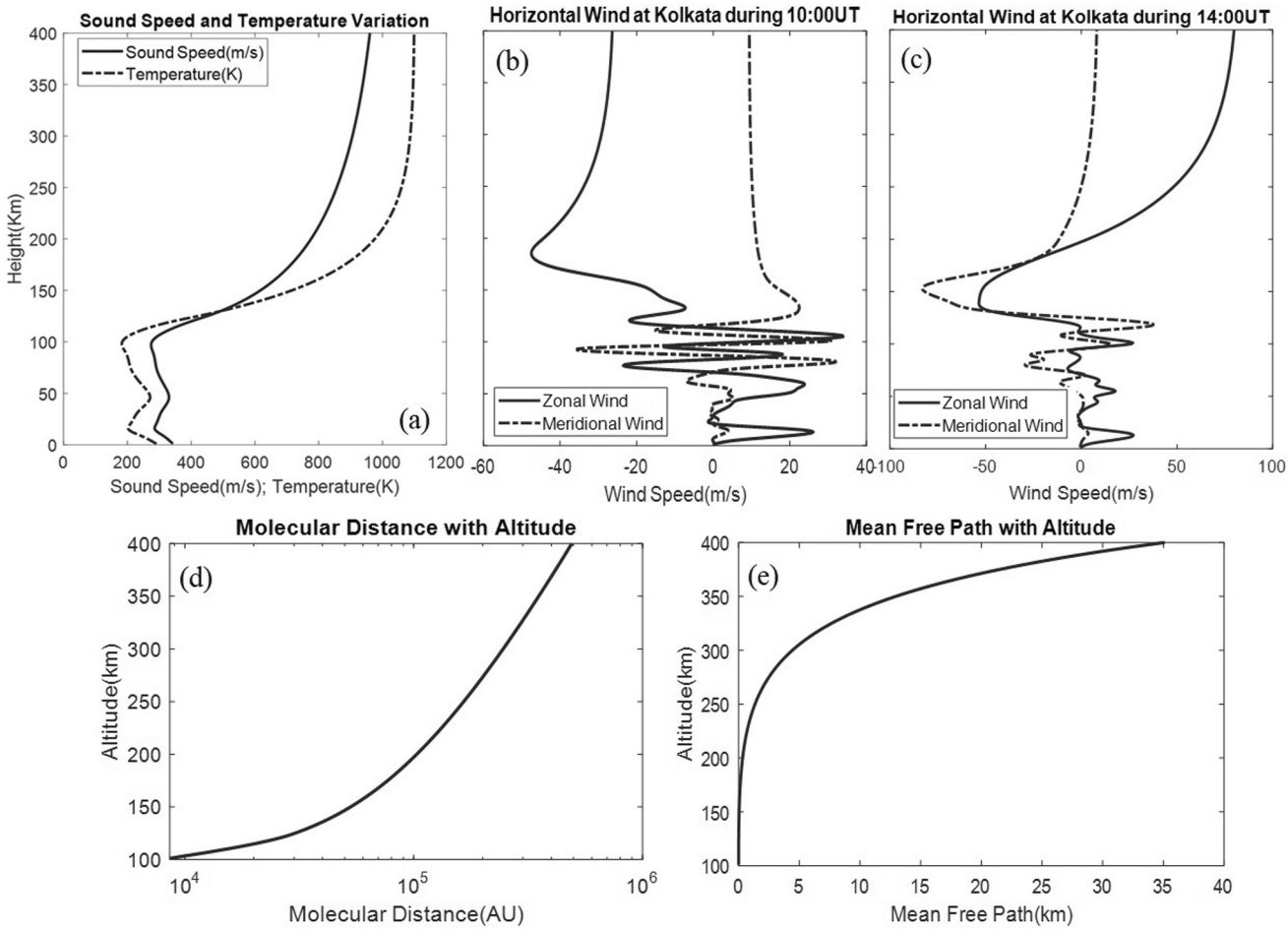

Figure 4. Background atmospheric parameters variations with altitude over Kolkata; (a) Sound speed and temperature variation with altitude; (b) and (c) Horizontal speed both in zonal and meridional direction during 09:00 and 14:00 UTC respectively; (d) and (e) Variation of molecular distance and mean free path with altitude.

detailed investigation was carried out by (Vadas & Crowley, 2017; Vadas et al., 2019) on the sensitivity of these parameters on GW propagation. The thermal diffusivity is measured by using $\kappa = \nu/\mathrm{Pr}$; where, Pr is the Prandtl number which is kept constant (0.62) for the entire process (Vadas, 2007; Vadas & Fritts, 2005).

3.3. Concentric Gravity Wave

Concentric GW is the theoretical representation of GWs which are generated from a point source and a small part of these waves reaches the ionosphere where circular or semi-circular rings of TIDs can be observed as a consequence of interactions between neutral waves and plasma. Vadas and Azeem (2021) has given a beautiful pictorial representation of conical shaped phase surface for upward propagating wave. The expressions for the basic parameters of the conical shaped wave structure have been given in details by Chou et al. (2017), Vadas and Azeem (2021).

The intrinsic frequency of a linear GW in isothermal and windless background condition can be defined as (Hines, 1960):

$$\omega_{ir} = N_B * \cos\Psi \tag{2}$$

N_B is the buoyancy frequency Ψ is the angle of GW propagation with respect to the zenith. If we express Equation 2 based on the concentric rings of observation then it can be written as (Vadas & Azeem, 2021):

$$\omega_{ir} = \frac{N_B}{\sqrt{1 + \frac{r^2}{\Delta h^2}}} \tag{3}$$

r is the radius of concentric ring of observation and Δh is the difference between observation and source altitude. The vertical wavelength and horizontal phase velocity are respectively expressed as:

$$\lambda_z = \frac{2\pi |v_z|}{N_B} \sqrt{\left[1 + \frac{r^2}{\Delta h^2}\right]} \tag{4}$$

$$v_h = 2\pi |v_z| \sqrt{\left[1 + \frac{r^2}{\Delta h^2}\right]} \tag{5}$$

where, $v_z\left(\approx \frac{\omega_i * \lambda_z}{2\pi}\right)$ is the vertical group velocity in isothermal and windless background condition and assumed as uniform for a small zone of observation. The relations indicate that period of propagation, vertical wavelength and horizontal phase velocity vary linearly with radial distance form the center of the ring if $r \gg \Delta h$. On the other hand, using Boussinesq approximation the dispersion relation for intrinsic frequency can be expressed as (Marks & Eckermann, 1995):

$$\omega_{ir}^2 = \frac{k_h^2 * N_B^2}{k_h^2 + k_z^2 + \frac{1}{4H^2}} \tag{6}$$

k_h and k_z are horizontal and vertical wave number where $k_h^2 = k_x^2 + k_y^2$; k_x and k_y are zonal and meridional wave number respectively. H is the vertical density scale height. ω_i varies with wind speed and its direction based on the relation:

$$\omega_{ir} = \omega_r - k_x U_x - k_y U_y \tag{7}$$

where, ω_r is the observed relative frequency; U_x and U_y are the zonal and meridional components respectively of background wind.

3.4. Ray Tracing Algorithm

Our ray tracing algorithm is based on the Lighthill Equations (Lighthill, 1978) in varying background wind and temperature(Eckermann, 1992; Marks & Eckermann, 1995):

$$\frac{dx_i}{dt} = U_i + \frac{\delta \omega_{ir}}{\delta t} \tag{8}$$

$$\frac{dk_i}{dt} = -\sum_{j=1}^{3} k_j \frac{\delta U_j}{\delta t} + \frac{\delta \omega_{ir}}{\delta t} \tag{9}$$

here, i,j = 1,2,3 which represent zonal, meridional and vertical directions respectively. Further, kinematic viscosity and thermal diffusivity have been incorporated in the wave propagation dispersion relations (Vadas & Fritts, 2005) and ion drag and wave induced diffusion are neglected as a suitable assumption of GWs with period less than an hour. Instead of using perturbation expansion in kinematic viscosity, this solution is more accurate in strong dissipation for the high frequency GW because of very high temperature and its higher gradient in thermosphere. The initial or observation altitude is chosen 290 km. The primary wave properties such as relative frequency (τ_r) and phase velocity(V_p), are determined based on the best fit relation with radial distance (as shown in Figure 7c for the case of phase velocity). The horizontal wavelength has been determined by $\lambda_h = \frac{V_p}{\tau_r}$ (Vadas & Azeem, 2021). Now intrinsic period (τ_{ir}) and vertical wavelength (λ_z) are retrieved from iterative solution to satisfy the GW dispersion relation with keeping V_p constant.

The dispersion relation for vertical wave number can be expressed as (Vadas, 2007; Vadas & Fritts, 2005; Vadas & Nicolls, 2009):

$$k_z^2 = \frac{k_h^2 N_B^2}{\omega_{ir}^2\left(1+\delta_+ + \delta^2/\mathrm{Pr}\right)}\left[1+\left(\frac{\nu}{2\omega_{ir}}\right)^2\left(k^2-\frac{1}{4H^2}\right)^2\frac{\left(1-\mathrm{Pr}^{-1}\right)^2}{\left(1+\delta_+/2\right)^2}\right]^{-1} - k_h^2 - \frac{1}{4H^2} \tag{10}$$

where, $k = \sqrt{k_h^2 + k_z^2}$); ν is kinematic viscosity which is the ratio of molecular viscosity and the neutral density; Pr is Prandtl number and it has been incorporated in the dispersion equations for the effect of thermal diffusivity and all the details have been described by (Vadas & Fritts, 2005, 2006). $\delta = \frac{\nu * k_z}{H * \omega_{ir}}$; $\delta_+ = \delta\left(1+\frac{1}{\mathrm{Pr}}\right)$. k_z at the initial altitude is computed based on the following iterative solution due to significantly large ν and dissipation effect:

$$k_z = \sqrt{\left(\frac{k_h N_B}{2H\nu}\right)^{\frac{2}{5}} k_z^{\frac{2}{5}} - k_h^2 - \frac{1}{4H^2}} \tag{11}$$

the first assumption for k_z of the right hand side of Equation 11 has been computed by:

$$k_z = \sqrt{\sqrt{\frac{k_h N_B}{2H\nu}} - k_h^2 - \frac{1}{4H^2}} \tag{12}$$

After estimation of wave parameters at the observation altitude the ray paths are extracted based on the reverse ray tracing mechanism. Here, eastward waves are considered with azimuth angle range from 40° to 140°assuming less dissipative force from viscosity due to wind effect and can propagate to the middle and upper thermosphere and generate significant amount of TIDs (Fritts & Vadas, 2008; Hocke & Schlegel, 1996; Vadas & Azeem, 2021).

The ray tracing algorithm also involves complex intrinsic frequency, proposed by Vadas and Fritts (2005), instead of complex wave number which is used in classic propagation theory by Pitteway and Hines (1963). It gives the realization of time dependent amplitude decay which provides the accurate solution of both μ and ν with time and space.This decay rate with time can be determined based on the imaginary part of the intrinsic frequency and it can be expressed as(Vadas & Fritts, 2005, 2006):

$$\omega_{Ii} = -\frac{\nu}{2}\left[k^2 - \frac{1}{4H^2}\right]\left[\frac{1+(1+2\delta)/\mathrm{Pr}}{1+\delta_+/2}\right] \tag{13}$$

The application of ray tracing eqs. provides the possible reverse ray path from the observation location in both horizontal and vertical direction. Since the study also investigated the role of kinematic viscosity under low wind filtering effect, the neutral component perturbations were measured along the ray paths. The perturbations in neutral atmospheric components along the ray path can be computed from momentum flux measurement which is expressed as (Vadas, 2007; Vadas & Fritts, 2009):

$$U_h' U_z^{*\prime}(\mathbf{x}, t) = \left|U_h' U_z'(\mathbf{x}, t)\right|_{t=t_0} * \frac{\rho(z_0)}{\rho(z)} * \exp\left(-\int_{t_0}^{t} \omega_{Ii}\, d\tau\right) \tag{14}$$

U_h' and $U_z^{*\prime}$ are the horizontal and vertical perturbed velocities. t_0 is the time of initial measurement. $\rho(z)$ is the atmospheric neutral density at the altitude of "z." Since the decay rate changes with space and time, it needs to be integrated along the ray path from the initial measurement to the observation and its spectral density can be obtained in its Fourier domain. The horizontal momentum flux is a crucial factor in ray tracing as well as to determine the dissipation altitude because it increases significantly and reaches its maximum at the dissipation altitude. But after it reaches to the dissipation altitude it decreases rapidly (Vadas & Azeem, 2021; Vadas et al., 2019; Vadas & Fritts, 2009).

3.5. Roles of Kinematic Viscosity in Wave Propagation and Dissipation at Thermosphere

It is very well known fact that kinematic viscosity is a crucial component for neutral wave propagation at thermospheric altitude. Since the study has been done under geomagnetic calm condition the molecular viscosity of atomic oxygen is considered and it can be expressed as (Vadas & Crowley, 2017):

$$\mu = 3.34 \times 10^{-4} \times T^{0.71} \tag{15}$$

here T is the background atmospheric temperature. Kinematic viscosity $\nu = \mu/\rho$ and Pr is taken here 0.62 and minimal variation of it with altitude is neglected for our algorithm. ν increases rapidly above 200 km altitude due to rapid decease in neutral density. Besides, molecular distance and mean free paths are also significant above 200 km altitude. The factor causes notable discrepancies in the ray tracing results. Hence, for dealing with these issues and for ray tracing results to follow the TID measurements the concept of decreasing μ has been incorporated and its sensitivity has been tested in detail (Vadas & Crowley, 2017). The rate of decrease is controlled by two components Z_μ and β in the following way:

$$\mu = \begin{cases} 3.34 \times 10^{-4} \times T^{0.71}, & \text{if } Z < Z_\mu \\ \mu(Z_\mu)\left(\dfrac{\rho}{\rho(Z_\mu)}\right)^{\beta/3}, & \text{if } Z > Z_\mu \end{cases} \tag{16}$$

Z_μ is the altitude from where μ starts decreasing and β is an unknown factor which controls the rate of decrease and need to be estimated. The values of Z_μ are kept between 220 and 260 km since, bellow 220 km altitude TID measurements follow well with the measurements of μ by using Equation 16. On the other hand, choosing Z_μ above 270 km is avoided because the observed waves can't reach the observation altitude for $Z_\mu > 270$ km. Now, the decrease of μ still allow the kinematic viscosity to increase (except $\beta \geq 3$) which is capable of dissipating the observed waves in middle and upper thermospheric altitude. Figure 5 Shows the variation of both molecular and kinematic viscosity with respect to altitude at 10:00 UTC for two different Z_μ (220 and 250 km) and three different values of β (1, 1.5, and 2). The mathematical expressions and figures indicate that with increasing Z_μ both μ and ν increases whereas β has the opposite effect. Further the sensitivity of this Z_μ and β on the altitude of maximum perturbation is tested over the study location.

4. Results and Discussion

4.1. Linear Increase of Phase Velocity From Thunderstorm Location

A detailed investigation has been done based on the eastward TIDs of significant amplitude. Higher frequency (greater than 4 mHz) TID components are considered as acoustic wave signatures and hence excluded for this study as suggested by (Eckermann, 1992; Marks & Eckermann, 1995). After excluding the acoustic wave signatures TID maps are constructed based on dTEC signatures at available IPP locations. Figure 6 indicates the dTEC map over the study location based on the available IPP points. A spatial interpolation at a resolution of $0.5° \times 0.5°$ has been carried out covering the region over the available IPP points. Green function based 2D spline interpolation was performed using MATLAB. Unfortunately, the entire observation area (shaded in Figure 6) could not be studied due to data unavailability. A small area has been shown here having available IPP points. Figures 6a and 6b indicates the dTEC map during normal condition (i.e., no geomagnetic disturbances and thunderstorm activities). No such noteworthy variation was observed during the said period and the dTEC amplitude also varied within $\pm 0.15 TECU$. On the other hand a significant dTEC variation observed on April 1 (Figures 6c and 6d). It is also interesting to observe from the interpolated TID map that the consecutive +ve and −ve phases of TID variations followed almost a circular pattern. The fitted circular rings (red circles) are drawn based on these circle-like patterns both for +ve and −ve phase of the TIDs. Moreover all these fitted circular rings were almost concentric and situated very close to the region where maximum number lightning strikes were marked. Further investigations have also been carried out to verify that the observed TIDs follow the properties of concentric TIDs.

TID signatures based on satellite IPP trajectories of various azimuth angles during 10:30 UTC to 12:30 hr are shown in Figure 7. The intrinsic period, horizontal wavelength(wave number) and phase velocities of the TIDs are

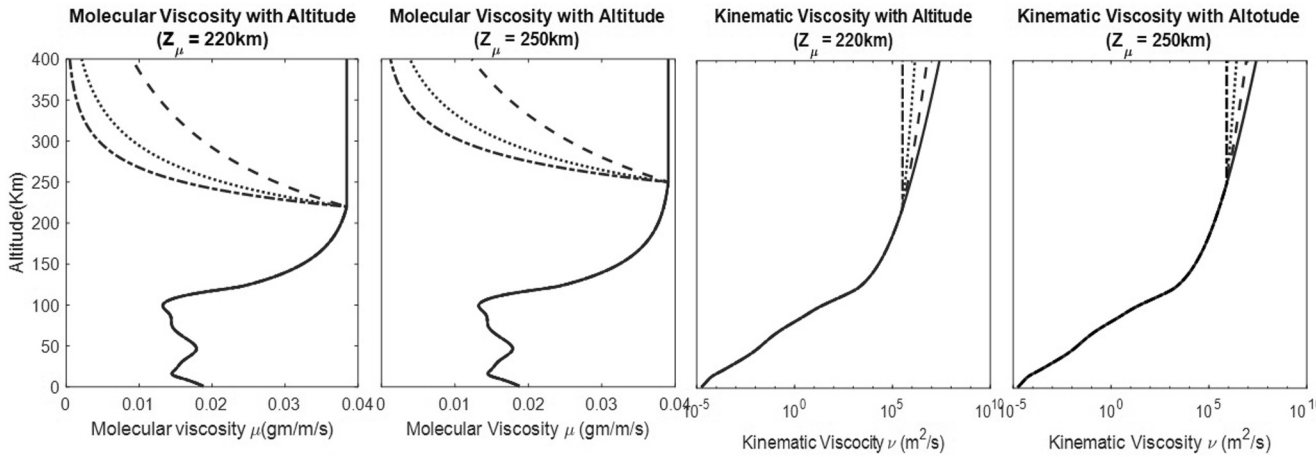

Figure 5. Molecular and Kinematic viscosity at the study location during 10:00 UTC(Local time 15:30 hr) for $Z_\mu = 220$ and 250 km. Solid, dash, dot, dash-dot lines are for $\beta = 0,1,2,3$ respectively.

calculated based on the measurements by three closely spaced receivers ($X_1(x_1, y_1, z_1)$, $X_2(x_2, y_2, z_2)$, $X_3(x_3, y_3, z_3)$) (Hernndez-Pajares et al., 2012; Oluwadare et al., 2022; Vadas & Fritts, 2005; M. Wang et al., 2007):

$$k_x = \frac{y_{21}\phi_{31} - y_{31}\phi_{21}}{x_{31}\,y_{21} - x_{21}\,y_{31}}; k_y = \frac{x_{21}\phi_{31} - x_{31}\phi_{21}}{x_{21}\,y_{31} - x_{31}\,y_{21}} \tag{17}$$

$$\text{Horizontal wavelength}(\lambda_h) = \frac{2\pi}{\sqrt{k_x^2 + k_y^2}} \tag{18}$$

ϕ_{21} and ϕ_{31} are phase difference of TIDs between X_2–X_1 and X_3–X_1 respectively. The azimuth angle of propagation can be computed as:

$$\Omega = \arctan\frac{t_{21}X_{31}\cos\varphi_{31} - t_{31}X_{21}\cos\varphi_{21}}{t_{31}X_{21}\sin\varphi_{21} - t_{21}X_{31}\sin\varphi_{31}} \tag{19}$$

t_{21} and t_{31} are the time difference between X_2–X_1 and X_3–X_1 respectively which are computed based on maximum correlation measurement. φ_{21} and φ_{31} are azimuthal angle between X_2–X_1 and X_3–X_1 respectively which are measured along the anticlockwise direction from positive north. The phase velocity and period of the wave can be computed as:

$$V_{ph} = \frac{X_{21}}{t_{21}}\cos(\Omega - \varphi_{21}); T = \frac{V_{ph}}{\lambda_h} \tag{20}$$

A relatively high phase velocities of above 250 m/s with horizontal wavelength of 300 km were found in several observations. Figures 7a and 7b shows the phase velocities observed at different IPP location. It has also been noted that phase velocity increased with increasing the horizontal distance from the thunderstorm zone. Vadas and Azeem (2021) also reported that both phase velocity and period of the GW increases with radial distance if the waves are emitted from a single point source. The pattern of this increase shows linear in nature if radial distance is significanly large as compared to the altitude difference between source and observation. Hence, a further investigation has been carried out where phase velocities have been collected from three different distances along a nearly unique azimuth angles (~55°, 85°, and 130°; in clockwise direction from positive North) from a point (Lat: 22°N and Lon: 85.5°E). The point is selected based on significant number of lightning strikes during very initial phase of the thunderstorm system assuming it as a source of GW. Variation of horizontal phase velocity with radial distance is shown in Figure 7c. A nice linear relationship has been found between the measured phase velocities and the radial distance from all the measurements and interestingly all these measured values are lying

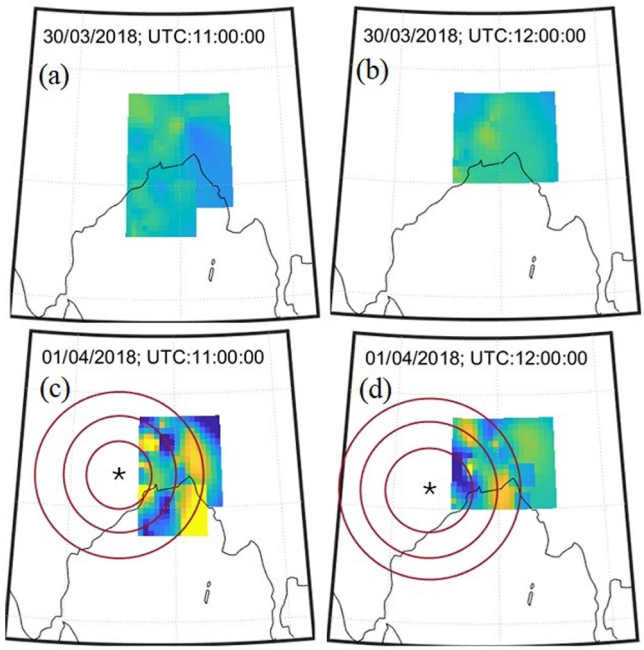

Figure 6. (a) and (b) dTEC variation over the study location on a clear day (30 March 2018) (c) and (d) dTEC variation on 1 April 2018 indicates the circular ring of TID.

within the 95% accuracy boundary from the best fitting line. The similar signatures also found in the experiment done by (Vadas & Azeem, 2021) where they mentioned the outcome as primary observation of concentric GW. The horizontal wavelength was also increasing with increasing radial distance. Vadas and Fritts (2009) reported that GWs generated from a point source have a widely varying horizontal and vertical wavelength. Vadas et al. (2012) reported that negligible wind filtering and dissipation effect shows the concentric rings of GWs at observation altitude. Xu et al. (2015) reported that from a point source the GWs can propagate a large distance without much varying its horizontal wavelength due to ducting effect.

4.2. Application of Ray Tracing

The ray tracing eqs. are applied on the eastward TID measurement in presence of varying temperature, atmospheric neutral particle density, wind in both temporal and spatial domain. Six different significantly high amplitude TIDs observed between 10:30 UTC to 12:30 UTC are used here. The wave parameters such as horizontal wavelength (λ_h) are measured based on the wave responses at the IPP locations of a satellite. Horizontal phase velocities and relative period are computed based on the linear fitting relation with radial distance, $\tau_r(2\pi/\omega_r) = \lambda_h/V_p$ and λ_z has been measured based on Equations 11 and 12. Now the possible ray path is primarily retrieved based on the Lighthill equations by using the wind measurement from HWM-14 model. The initial altitude is chosen as here 300 km based on the assumed IPP location of GPS satellites. The entire process is done based on implicitly in time domain and explicitly in spatial domain rather than implicitly in spatial domain and explicitly in time domain as suggested by previous literature.The time steps are taken such a way that the following conditions don't violate at any steps:

$$k_z > \frac{du_h/dz}{u_h}; k_z > \frac{dH/dz}{H}; k_z > \frac{d\nu/dz}{\nu} \tag{21}$$

The process generates a ray path which indicates the possible propagation track of the corresponding wave and the source can be located anywhere along the ray path.

4.2.1. Ray Tracing Sensitivity to Z_μ and β

A statistical study has been done to understand the role of β and Z_μ in the effective kinematic viscosity working on the wave propagation and further its dissipation. Assuming the higher amplitude TIDs within small arc (±0.5° azimuthal deviation) of satellite IPP location have almost similar properties. Here we have taken 12 samples with 1 min interval from seven different TIDs. The mean and standard deviation of basic initial properties such as horizontal wavelength, phase velocity and azimuth angle of propagation of the corresponding waves within each arc have been computed from the signatures of TIDs. Hence, we have defined 12 (12×7) different waves within each of seven groups. Further, the initial measurements of horizontal wavelength, phase velocity and azimuth angle of the waves within each group is computed based on the mean and standard deviation values within that group in the following way:

$$\lambda_H(i) = \overline{\lambda_H} + \Delta\lambda_H\left(-1 + \frac{2(i-1)}{n-1}\right); i = 1,2,3,\ldots..n \tag{22}$$

$$V_p(j) = \overline{V_p} + \Delta V_p\left(-1 + \frac{2(j-1)}{n-1}\right); j = 1,2,3,\ldots..n \tag{23}$$

$$\theta_{azm}(l) = \overline{\theta_{azm}}; l = 1,2,3,\ldots..n \tag{24}$$

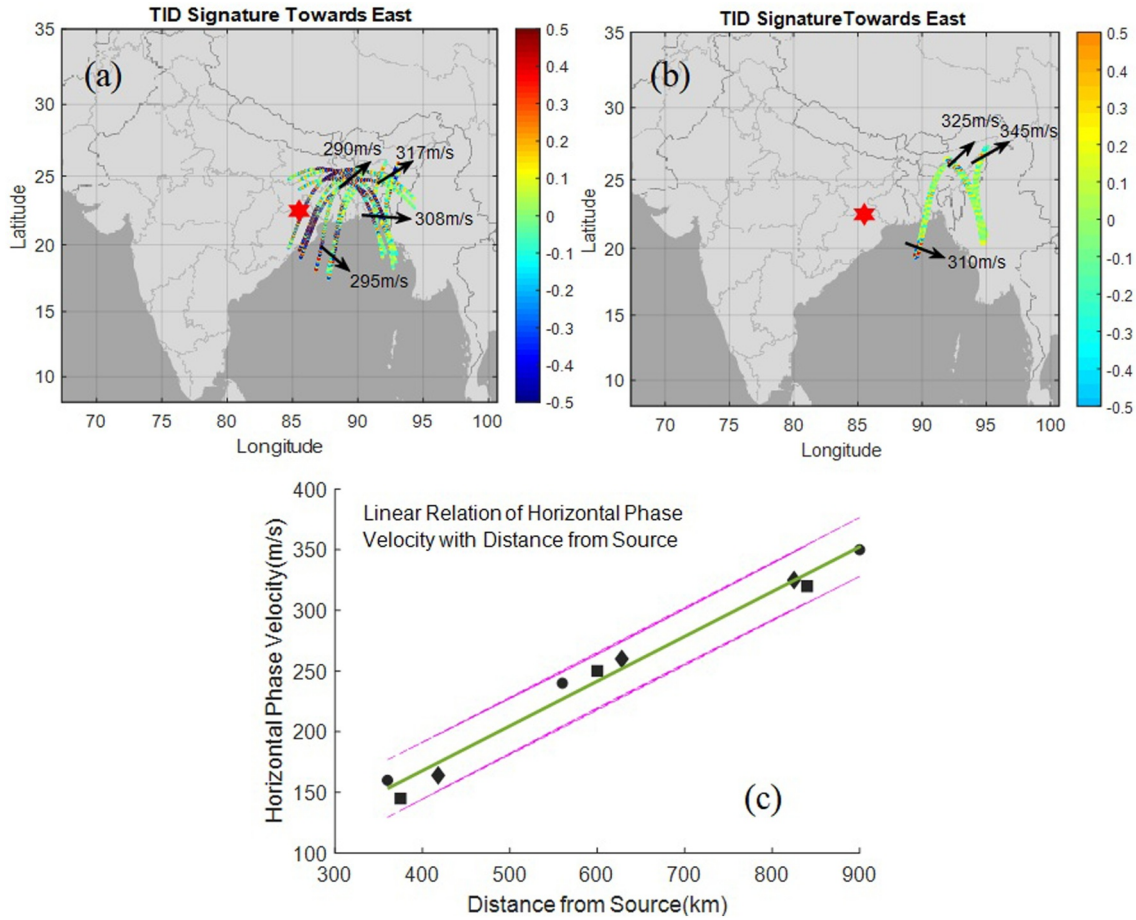

Figure 7. (a) and (b) Horizontal phase velocities observed during different time of the day at the IPP locations of the satellites (c) linear relation of phase velocities with radial distance from thunderstorm location.

As the samples are taken within a small range azimuthal deviation from the mean, the angle of propagation is considered constant for each group of 12 waves. The initial parameters of the waves before applying to the ray tracing algorithm, are listed in Table 1. It can be noted that the waves with a widely varying initial parameters (horizontal wavelengths were varying from 200 to 400 km whereas the phase velocities were varying from 150 to 360 m/s) have been considered for the statistical investigation. Now, all these waves are applied to ray tracing algorithm separately for varying λ_H (keeping V_p constant $\left(V_p = \overline{V_p}\right)$) and varying V_p (keeping λ_H constant $\left(\lambda_H = \overline{\lambda_H}\right)$). The initial altitude is kept 300 km and the ray tracing have been done with zero background wind and varying temperature. Wind velocity is kept zero because of two factors: (a) it is the key factor in wave dissipation but here the testing of effective ν based on the background temperature, Z_μ altitude and β is attempted; (b) the model wind plays a major role as a source of error in the measurements. The measurements of perturbation in horizontal velocity component based on the polarization relations have been done along the ray path and it reveal the wave dissipation altitude based on the altitude of maximum perturbation for each wave. The ray tracing computations of all waves have been done with respect to different values of ν by varying Z_μ and β to understand the roles of these two key components on the wave dissipation over the study location. Figures 6–8 shows the variation of altitude of maximum wave amplitude $\left(U_H'\right)$ with respect to initial λ_H and V_p based on the variation of Z_μ and β. Here, Z_μ has been considered as 230 , 245, and 250 km and three different values (1.0, 1.5, and 2.0) have been chosen for β. It has been found that the altitude of maximum U_H' varied in the range between 220

Table 1
Parameters of Gravity Wave Used for Ray Tracing Algorithm

Sl.No.	Azm.(degree)	τ_r (min)	V_p (m/s)	λ_h (km.)	Marker
1.	71	13.4	297.5 ± 31.7	254 ± 32.7	◇
2.	35	19.0	216.5 ± 36.6	227.35 ± 39	▷
3.	133.5	22.0	231.9 ± 78.3	297.1 ± 94	×
4.	55	20.3	314.1 ± 40	356.5 ± 26.3	□
5.	43.2	18	252.3 ± 22	303.8 ± 16.4	∘
6.	60	18	314.2 ± 21.6	259.5 ± 29.6	+
7.	82	18	293.7 ± 65.7	319.3 ± 72	*

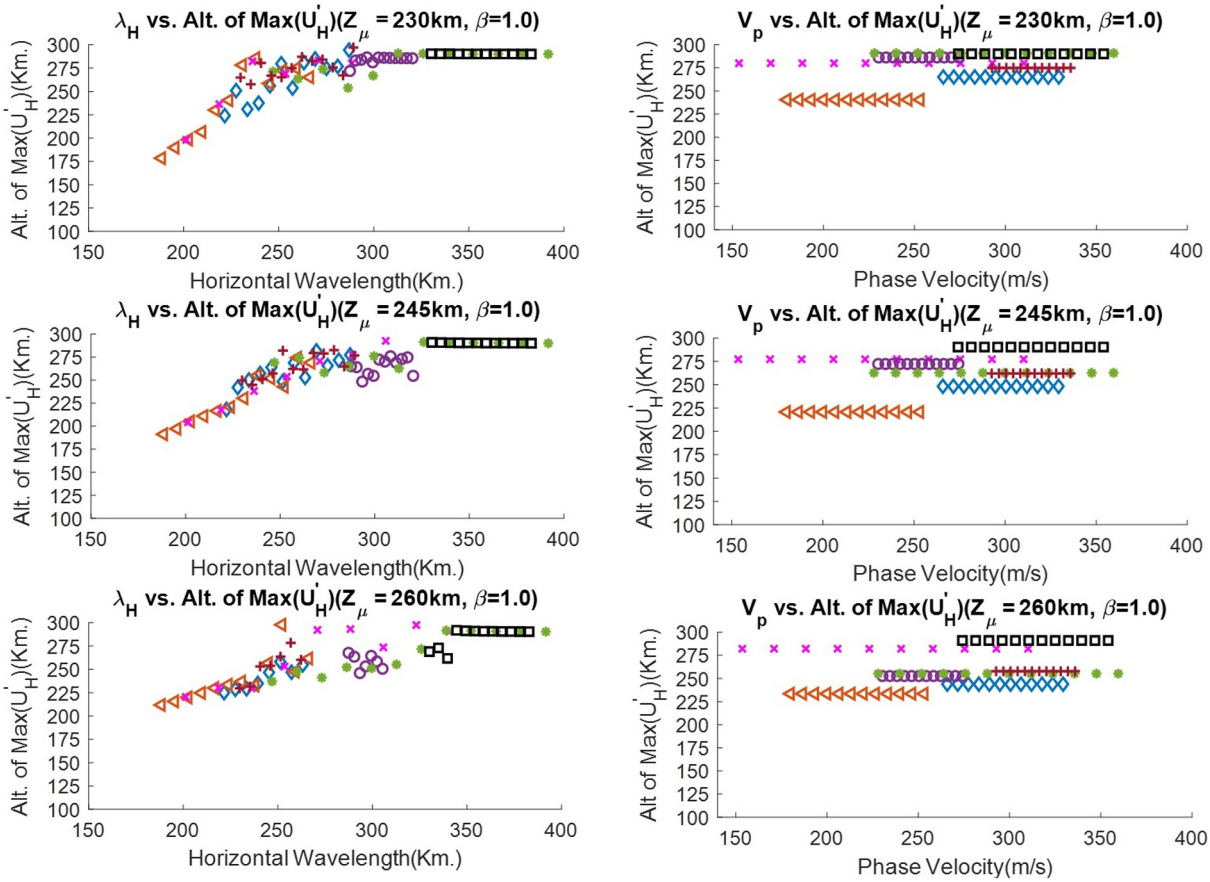

Figure 8. Horizontal wavelength and phase velocity of gravity waves at the maximum perturbation altitude with Z_μ = 230, 245, and 260 km and β = 1.0.

and 295 km altitude. Though, the maximum wave amplitudes have been found above 240 km and below 285 km for almost all samples but no strong decision can be taken on the possibility of altitude of maximum amplitude with this limited number of observation over the study location. It is also interesting to identify that with increasing Z_μ, by keeping β constant, the altitude of maximum U'_H decreased both for varying λ_z and varying V_p. This signatures are typically more substantial when Z_μ is varying from 230/245 to 260 km. It can be attributed by the condition of momentum flux to be maximum at isothermal background. The temperature variation above 230 km altitude is negligible and hence isothermal forms of wave propagation eqs. are needed to be considered above this altitude. The condition for the momentum flux to be maximum at the isothermal background condition can be expressed as (Vadas & Fritts, 2005):

$$\frac{\psi \nu H k^4}{|m|\omega_{Ir}} \simeq 1 \tag{25}$$

The relation indicates that, as ν increases with increasing Z_μ, the altitude of maximum U'_H should be lower for the validation of the condition of momentum flux to be maximum. On the other hand with increasing β and keeping Z_μ constant, the values of ν reduce and hence the altitude of maximum perturbation will increase. The above postulates in isothermal background condition are reflected very well in the observations as shown in Figures 8–10. Another interesting observation it has been found that an almost constant maximum perturbation altitude has been detected for Z_μ = 230 km and β = 2.0. The maximum perturbation occurred at almost 265 km altitude for almost all waves. The signatures are almost similar both for varying initial wavelength and phase velocities. The vertical wavelength measurements have been carried out for the waves with initial horizontal wavelengths and phase velocities as $\lambda_H = \overline{\lambda_H}$ and $V_p = \overline{V_p}$ respectively. The variations of these vertical wavelengths along the ray paths at zero background wind is shown in Figure 11. It is interesting to observe that from lower altitude they

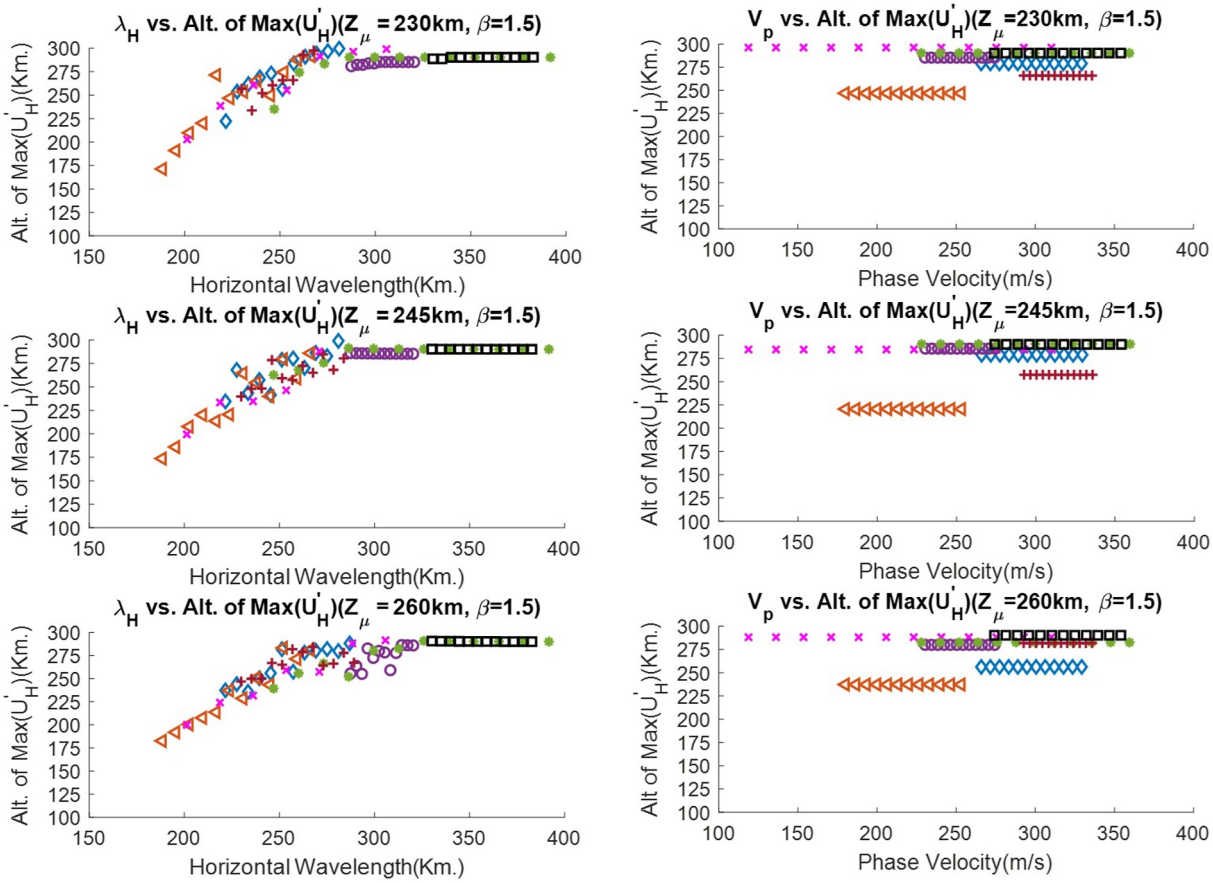

Figure 9. Horizontal wavelength and phase velocity of gravity waves at the maximum perturbation altitude with Z_μ = 230, 245, and 260 km and β = 1.5.

increased rapidly and reached the maximum at about 265 km altitude. After that they started decreasing and saturated about 300 km altitude. The ray tracing validation is tested based on the residual measurements from the vertical wave number variations with altitude as(Vadas & Crowley, 2017; Vadas & Fritts, 2005):

$$R3 = \frac{1}{2k_z^3}\frac{d^2k_z}{dz^2} - \frac{3}{4k_z^4}\left(\frac{dk_z}{dz}\right)^2 \tag{26}$$

The residual measurement below 1 along the ray path confirms the validation of WKB approximation (Einaudi & Hines, 1970) and it also assures that wave is not dissipating or reflecting. It has been found from observed vertical wavelegths that the magnitude of residual below 1 was continuing up to 305 km altitude which is almost one scale height above the altitude maximum vertical wavelength. Vadas (2007) reported that the wave can be observed 1–2 scale height above the altitude maximum momentum flux or the altitude of maximum vertical wavelength. This is also reflected in our observations of momentum flux measurements with kinematic viscosity with Z_μ = 230 km and β = 2.0 and the measurements of vertical wavelength with zero background wind.

4.2.2. Estimation of Source Location Using Ray Tracing Algorithm

Figure 10 shows the outcome of reverse ray tracing of six high amplitude TIDs both in zero and HWM model background wind. Z_μ and β are chosen 230 km and 2.0 respectively for measurement of effective ν. Initial altitude is fixed to 290 km as WKB approximation and hence ray tracing validation fails almost 300 km altitude. The starting location of each associated GW is marked with black square. The possible propagation path of each GW is shown by individual colored reverse ray tracing line both in horizontal and vertical direction. Figures 12a and 12b indicates the possible propagation paths in zero background wind. The source can

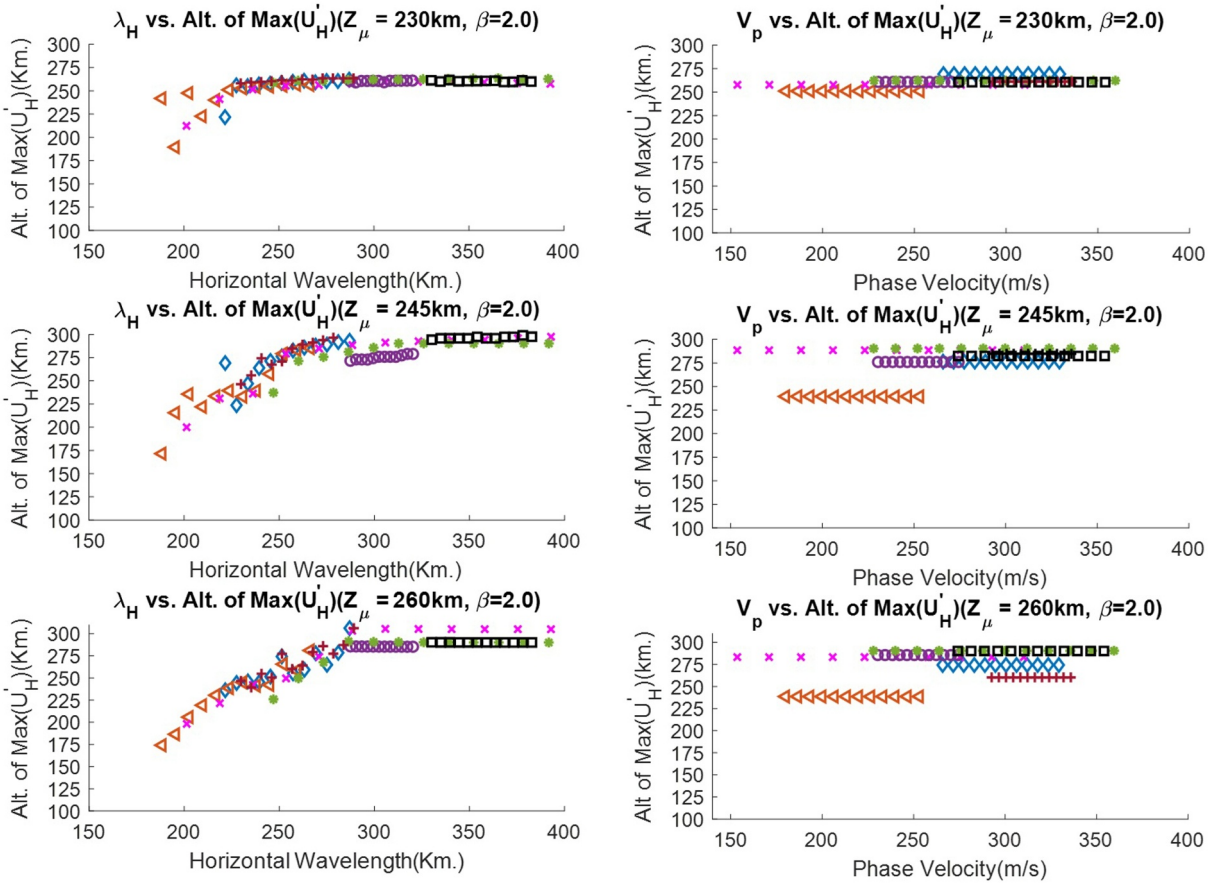

Figure 10. Horizontal wavelength and phase velocity of gravity waves at the maximum perturbation altitude with Z_μ = 230,245, and 260 km and β = 2.0.

be anywhere along the horizontal line. It is interesting to identify a common crossing point of all possible ray paths and the point was very near to our previously assumed source location and a significant number of lightning strikes also occurred there. Figure 12b shows the altitude measurement corresponding to each ray tracing line. The launching altitude is fixed as 290 km for all GWs and it is interesting to find that each measurement reaches the minimum possible altitude of ~127 km. After reaching to the minimum possible altitude it revert back to the upward direction and the measurements are stopped just before reaching the altitude where WKB approximation fails. The asterisks in horizontal propagation paths indicate the lowest altitude point in the corresponding vertical propagation paths. Figures 12c and 12d indicate the ray paths in HWM-14 model wind. The horizontal ray paths had almost single interaction point and the lowest altitude it reached almost 127 km for all waves in this case also. An interesting observation it has been found here that lowest altitude points of all waves came very close to the common interaction point with the incorporation of model wind. Hence, it can be assumed from the observations that all the GWs are generated by a single point source as all the tracking lines interacted to a single point source both in zero and nonzero background wind condition. The lowest altitude points which are closed to the common interaction point in presence of model background wind and found an almost unique minimum possible altitude which is situated at lower thermospheric height of ~127km.

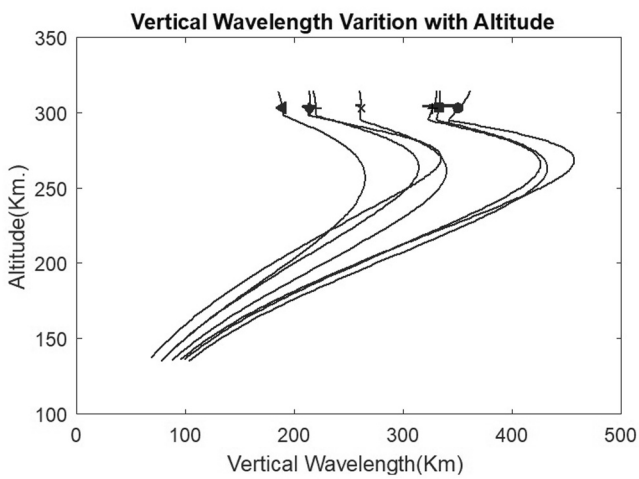

Figure 11. Vertical wavelength variations of the waves under zero wind.

The results indicated that the observed waves are possibly secondary waves. Now, GWs can't propagate (Vadas & Crowley, 2010) in the atmosphere if their intrinsic phase velocity exceeds the sound speed (C_s), whereas the

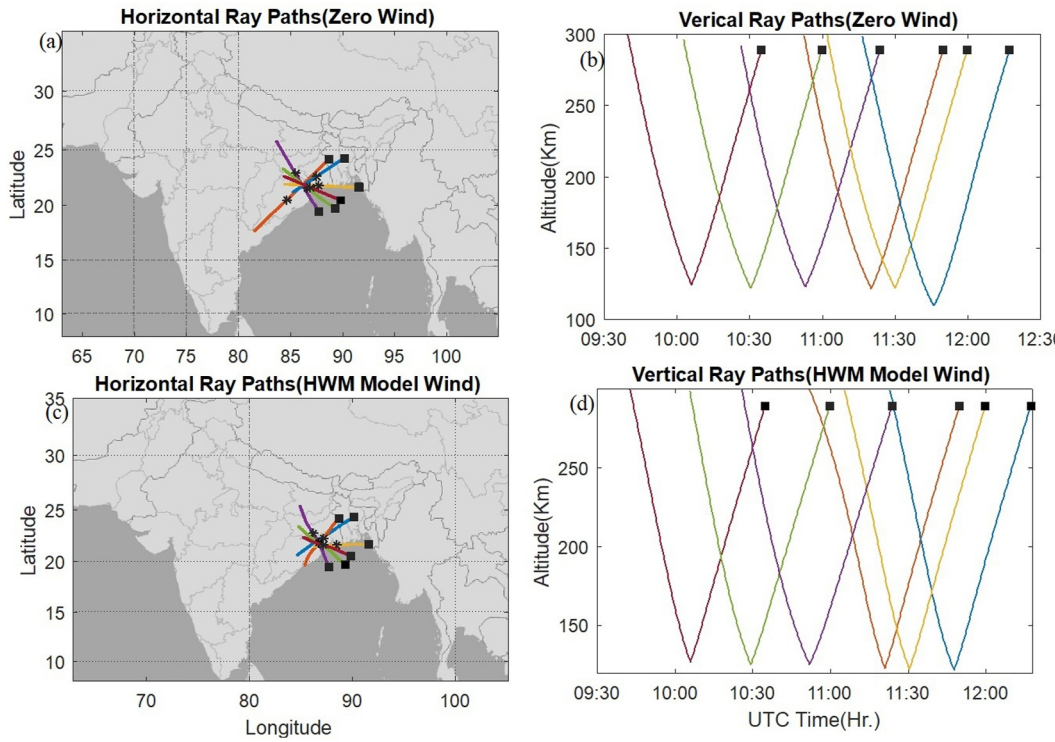

Figure 12. Ray tracing on six eastward gravity waves; (a) and (b) measurements in zero back ground wind indicating horizontal and vertical ray paths; (c) and (d) measurements in HWM-14 background wind indicating horizontal and vertical ray paths respectively.

maximum intrinsic speed of the waves can be determined as $\frac{2\sqrt{\gamma-1}}{\gamma}C_s$. Figure 4a suggests that minimum value of sound speed is 275 m/s which can be found below the turbopause at 98 km altitude. Hence, following the condition of maximum intrinsic phase velocity will be 247.5 m/s. Horizontal wind speed is $\simeq -12$ m/s. It indicates that the GW can propagate at a maximum $\simeq$260 m/s phase velocity over this region.

Figure 13 indicates the ratio of intrinsic phase velocity and $\frac{2\sqrt{\gamma-1}}{\gamma}C_s$ as a function of V_p and altitude along the three different propagation angles 45°, 90° and 135° at 10:00 UTC. Since, intrinsic phase velocity can't be more than $\frac{2\sqrt{\gamma-1}}{\gamma}C_s$ in normal condition, the ratio between these two components should not more than or equal to one (indicate by shaded region of Figure 13) without tunneling. It is indicative from Figure 13 that the waves with phase velocities more than 300 m/s can't go below the turbopause and the waves with phase velocities 250 m/s are unable to propagate through 90–110 km altitude without tunneling. The above observations indicate that the observed GWs were not directly involved with the convective system rather they were originated from secondary source at the thermospheric altitude.

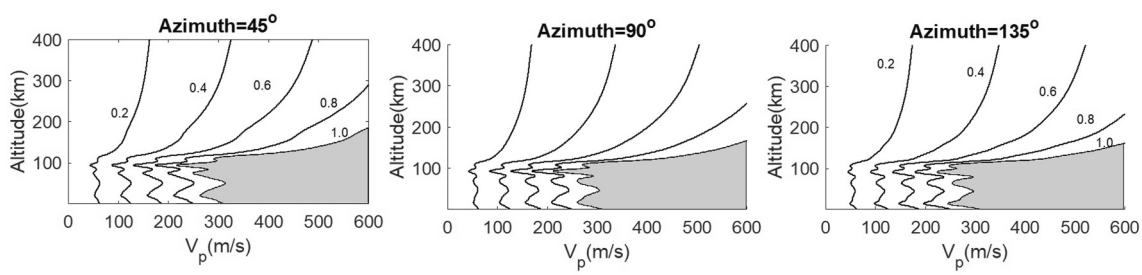

Figure 13. The ratio of horizontal intrinsic phase velocity (V_{Ip}) and $\frac{2\sqrt{\gamma-1}}{\gamma}C_s$ as the function of altitude and V_p at three different azimuth angles [45°, 90°, and 135°] during 10:00 UTC. The shaded region shows the ratio value ≥1.

It can be summarized from the observations that the GWs of which phase velocity linearly increased ($\simeq 150-350$ m/s) with the radius possibly have the same point source and the waves with phase velocity >260 m/s can not propagate below the turbopause (Vadas & Azeem, 2021). By considering these two conditions, it can be concluded that all the observed waves were originated from a single point source at thermospheric altitude.

5. Conclusion

The study has carried out a detailed analysis of convective system induced GW propagation above lower thermospheric altitude in tropical region. Results hinted toward the probable concentric sources for all the waves observed. The study retrieved the probable ray path from the observation altitude extending up to the altitude of WKB validation using ray tracing algorithm. The existence of concentric waves in this case was further validated by the results of ray tracing both with zero and modeled wind. Both GAGAN network installed by Airport Authority of India and UNAVCO network of GPS are used in detection of convection generated AGWs. dTEC maps are constructed based on the available data points at IPP locations and using Green's function based spatial interpolation. The interpolated dTEC maps shows the consecutive +ve and −ve phases of TIDs which formed an almost circular rings and had a common center. TIDs observed in this case were found to have a horizontal wavelength of 300 km and a very high phase velocity of about 300 m/s which indicates the confinement of the wave above thermospheric heights. Both the phase velocity and period of propagation were observed to increase linearly with radial distance from the thunderstorm location. The horizontal wind speed is significantly small compared to the wave phase velocity. Hence, wind filtering effect is not much crucial on the wave propagation. It provides a nice opportunity to study the role of kinematic viscosity on wave propagation under small wind filtering effect. A statistical investigation was carried out based on forward propagation of the waves to find the role of kinematic viscosity on the observed waves. The study found a particular kinematic viscosity for which the observed waves dissipated at around 260 km altitude. Interestingly, the WKB approximation fails one scale height above the dissipation altitude which falls in line with the theories. Three-dimensional propagation paths of the observed waves are retrieved under both zero wind and model wind conditions by using this particular kinematic viscosity in ray tracing algorithm. All the horizontal ray paths were interacted at a common point under both the conditions and interestingly all the lowest altitude points almost coincided to that common interaction point. The investigation finds a better observation of the concentric GWs and their propagation under an unique kinematic viscosity. The study can be useful in understanding the role of effective kinematic viscosity in propagation and dissipation of low frequency atmospheric waves in tropical region.

Data Availability Statement

The GPS data has been collected from UNAVCO archive (https://www.unavco.org/data/gps-gnss/gps-gnss.html). We acknowledge Airport Authority of India for providing additional GPS data. We acknowledge Indian Space Research Organisation for cloud images which are collected from MOSDAC archive (www.mosdac.gov.in). Lightning strikes information has been collected World Wide Lightning Location Network (http://wwlln.net/).

Acknowledgments
Authors thankfully acknowledge The Environmental Panning and Coordination Organization for funding Soumen Datta under Chief Minister fellowship program for doing PhD on Climate Change. The authors gratefully acknowledge the Airport Authority of India (AAI), Ahmedabad for providing GPS GAGAN network data. Authors are also thankful to WWLLN for providing lightning data. Authors would like to acknowledge Indian Space Research Organisation (ISRO) for providing INSAT cloud images through Mosdac. Authors would also like to acknowledge UNAVCO for GPS data.

References

Alexander, M. J. (1996). A simulated spectrum of convectively generated gravity waves: Propagation from the tropopause to the mesopause and effects on the middle atmosphere. *Journal of Geophysical Research*, *101*(D1), 1571–1588. https://doi.org/10.1029/95JD02046

Alexander, P., Delatorre, A., Schmidt, T., Llamedo, p., & Hierro, R. (2015). Limb sounders tracking topographic gravity wave activity from the stratosphere to the ionosphere around midlatitude Andes. *Journal of Geophysical Research: Space Physics*, *120*(10), 9014–9022. https://doi.org/10.1002/2015JA021409

Andrews, D. G., Leovy, c. B., & Holton, J. R. (1987). *Middle atmosphere dynamics* (p. 489). Academic Press.

Azeem, I., Vadas, S. L., Crowley, G., & Makela, J. J. (2017). Traveling ionospheric disturbances over the United States induced by gravity waves from the 2011 Tohoku tsunami and comparison with gravity wave dissipative theory. *Journal of Geophysical Research: Space Physics*, *122*(3), 3430–3447. https://doi.org/10.1002/2016JA023659

Azeem, I., Yue, J., Hoffmann, L., Miller, S. D., Starka, W. C., & Crowley, G. (2015). Multisensor profiling of a concentric gravity wave event propagating from the troposphere to the ionosphere. *Geophysical Research Letters*, *42*(19), 7874–7880. https://doi.org/10.1002/2015GL065903

Burrell, A. G., Bonito, N. A., & Carrano, C. S. (2009). Total electron content processing from GPS observations to facilitate ionospheric modeling. *GPS Solutions*, *13*(2), 83–95. https://doi.org/10.1007/s10291-008-0102-3

Chou, M. Y., Lin, C. C. H., Yue, J., Tsai, H. F., Sun, Y. Y., Liu, J. Y., & Chen, C. H. (2017). Concentric traveling ionosphere disturbances triggered by Super Typhoon Meranti (2016). *Geophysical Research Letters*, *44*(3), 1219–1226. https://doi.org/10.1002/2016GL072205

Cole, K. D., & Hickey, M. P. (1981). Energy transfer by gravity wave dissipation. *Advances in Space Research*, *1*(12), 6574–6575. https://doi.org/10.1016/0273-1177(81)90418-X

Datta, S., & Das, S. (2023). Signature of thunderstorm induced acoustic and gravity waves at low latitude Indian sector. *Advances in Space Research*, *73*(7), 3472–3485. https://doi.org/10.1016/j.asr.2023.09.018

Du, Y., Rotunno, R., & Zhang, F. (2019). Impact of vertical wind shear on gravity wave propagation in the land–sea-breeze circulation at the equator. *Journal of the Atmospheric Sciences*, *76*(10), 3247–3265. https://doi.org/10.1175/JAS-D-19-0069.1

Eckermann, S. D. (1992). Ray-tracing simulation of the global propagation of inertia gravity waves through the zonally averaged middle atmosphere. *Journal of Geophysical Research*, *97*(D14), 15849–15866. https://doi.org/10.1029/92JD01410

Einaudi, F., & Hines, C. O. (1970). Wkb approximation in application to acoustic-gravity waves. *Canadian Journal of Physics*, *48*(12), 1458–1471. https://doi.org/10.1139/p70-185

Figueiredo, C. A. O. B., Wrasse, C. M., Vadas, S., Takahashi, H., Otsuka, Y., Nyassor, P. K., et al. (2023). Daytime medium scale traveling ionospheric disturbances (MSTIDS) over the Andes mountains at equatorial and low magnetic latitudes. *Journal of Geophysical Research: Space Physics*, *128*(10), e2023JA031477. https://doi.org/10.1029/2023JA031477

Fritts, D. C., & Alexander, M. J. (2003). Gravity wave dynamics and effects in the middle atmosphere. *Reviews of Geophysics*, *41*(1), 1003. https://doi.org/10.1029/2001RG000106

Fritts, D. C., & Vadas, S. L. (2008). Gravity wave penetration into the thermosphere: Sensitivity to solar cycle variations and mean winds. *Annals of Geophysics*, *26*(12), 3841–3861. https://doi.org/10.5194/angeo-26-3841-2008

Heale, C. J., Snively, J. B., Hickey, M. P., & Ali, C. J. (2014). Thermospheric dissipation of upward propagating gravity wave packets. *Journal of Geophysical Research: Space Physics*, *119*(5), 3857–3872. https://doi.org/10.1002/2013JA019387

Hernndez-Pajares, M., Juan, J. M., & Sanz, J. (2006). Medium-scale traveling ionospheric disturbances affecting GPS measurements: Spatial and temporal analysis. *Journal of Geophysical Research*, *111*(A7), A07S11. https://doi.org/10.1029/2005JA011474

Hernndez-Pajares, M., Juan, J. M., Sanz, J., & AragÃngel, A. (2012). Propagation of medium scale traveling ionospheric disturbances at different latitudes and solar cycle conditions. *Radio Science*, *47*(6), RS0K05. https://doi.org/10.1029/2011RS004951

Hickey, M. P., & Coley, K. D. (1988). A numerical model for gravity wave dissipation in the thermosphere. *Journal of Atmospheric and Terrestrial Physics*, *50*(8), 689–697. https://doi.org/10.1016/0021-9169(88)90032-3

Hines, C. O. (1960). Internal atmospheric gravity waves at ionospheric heights. *Canadian Journal of Physics*, *38*(11), 1441–1481. https://doi.org/10.1139/p60-150

Hines, C. O. (1974). Atmospheric gravity waves: A new toy for the wave theorist, in the upper atmosphere in motion. *Geophysical Monograph Series*, *18*, 198–206. https://doi.org/10.1029/GM018p0198

Hocke, K., & Schlegel, K. (1996). A review of atmospheric gravity waves and traveling ionospheric disturbances: 1982–1995. *Annals of Geophysics*, *14*(9), 917–940. https://doi.org/10.1007/s00585-996-0917-6

Horinouchi, T., Nakamura, T., & Kosaka, J.-I. (2002). Convectively generated mesoscale gravity waves simulated throughout the middle atmosphere. *Geophysical Research Letters*, *29*, 21. https://doi.org/10.1029/2002GL016069

Kaplan, E. D., & Hagerty, C. (2006). *Understanding GPS: Principles and applications* (2nd ed.). Artech House.

Lane, T. P., & Sharman, R. D. (2006). Gravity wave breaking, secondary wave generation, and mixing above deep convection in a three-dimensional cloud model. *Geophysical Research Letters*, *33*(23), L23813. https://doi.org/10.1029/2006GL027988

Lay, E. H., Shao, X.-M., & Carrano, C. (2013). Variation in total electron content above large thunderstorms. *Geophysical Research Letters*, *40*(10), 1945–1949. https://doi.org/10.1002/grl.50499

Lay, E. H., Shao, X. M., Kendrick, A. K., & Carrano, C. S. (2015). Ionospheric acoustic and gravity waves associated with midlatitude thunderstorms. *Journal of Geophysical Research: Space Physics*, *120*(7), 6010–6020. https://doi.org/10.1002/2015JA021334

Lighthill, J. (1978). *Waves in fluids*. Cambridge Univ. Press.

Marks, C. J., & Eckermann, S. D. (1995). A three-dimensional nonhydrostatic ray-tracing model for gravity waves: Formulation and preliminary results for the middle atmosphere. *Journal of the Atmospheric Sciences*, *52*(11), 1959–1984. https://doi.org/10.1175/1520-0469(1995)052⟨1959:ATDNRT⟩2.0.CO;2

Munro, G. H. (1948). Short-period changes in the f region of the ionosphere. *Nature*, *162*(4127), 886–887. https://doi.org/10.1038/162886a0

Nishioka, M., Tsugawa, T., Kubota, M., & Ishii, M. (2013). Concentric waves and short-period oscillations observed in the ionosphere after the 2013 Moore EF5 tornado. *Geophysical Research Letters*, *40*(21), 5581–5586. https://doi.org/10.1002/2013GL057963

Occhipinti, G., Kherani, E. A., & Lognonne, P. (2008). Geomagnetic dependence of ionospheric disturbances induced by tsunamigenic internal gravity wave. *Geophysical Journal International*, *173*(3), 753765. https://doi.org/10.1111/j.1365-246X.2008.03760.x

Oluwadare, T. S., Jakowski, N., Valladares, C. E., Akala, O.-O. A., Abe, O. E., Alizadeh, M. M., & Schuh, H. (2022). Climatology of medium-scale traveling ionospheric disturbances (MSTIDS) observed with GPS networks in the North African region. *Pure and Applied Geophysics*, *179*(6–7), 2501–2522. https://doi.org/10.1007/s00024-022-03028-6

Picone, J. M., Hedin, A. E., Drob, D. P., & Aikin, A. C. (2002). Nrlmsise-00 empirical model of the atmosphere: Statistical comparisons and scientific issues. *Journal of Geophysical Research*, *107*(A12), 1468. https://doi.org/10.1029/2002JA009430

Pitteway, M. L. V., & Hines, C. O. (1963). The viscous damping of atmospheric gravity waves. *Canadian Journal of Physics*, *41*(12), 1935–1948. https://doi.org/10.1139/p63-194

Rahmani, Y., Mahdi Alizadeh, M., Schuh, H., Wickert, J., & Tsai, L. C. (2020). Probing vertical coupling effects of thunderstorms on lower ionosphere using GNSS data. *Advances in Space Research*, *66*(8), 1967–1976. https://doi.org/10.1016/j.asr.2020.07.018

Richmond, A. (1978). Gravity wave generation, propagation, and dissipation in the thermosphere. *Journal of Geophysical Research*, *83*(A9), 4131–4145. https://doi.org/10.1029/JA083iA09p04131

Tinmaker, M. I. R., & Chate, D. M. (2013). Lightning activity over India: A study of east-west contrast. *International Journal of Remote Sensing*, *34*(16), 5641–5650. https://doi.org/10.1080/01431161.2013.794987

Tsugawa, T., Otsuka, Y., Coster, A. J., & Saito, A. (2007). Medium-scale traveling ionospheric disturbances detected with dense and wide TEC maps over North America. *Geophysical Research Letters*, *34*(22), 5641–5650. https://doi.org/10.1029/2007GL031663

Vadas, S. L. (2007). Horizontal and vertical propagation and dissipation of gravity waves in the thermosphere from lower atmospheric and thermospheric sources. *Journal of Geophysical Research*, *112*(A6), A06305. https://doi.org/10.1029/2006JA011845

Vadas, S. L., & Azeem, I. (2021). Concentric secondary gravity waves in the thermosphere and ionosphere over the continental United States on March 25–26, 2015 from deep convection. *Journal of Geophysical Research: Space Physics*, *126*(2), e2020JA028275. https://doi.org/10.1029/2020JA028275

Vadas, S. L., & Crowley, G. (2010). Sources of the traveling ionospheric disturbances observed by the ionospheric TIDDBIT sounder near Wallops island on 30 October 2007. *Journal of Geophysical Research*, *115*(A7), A07324. https://doi.org/10.1029/2009JA015053

Vadas, S. L., & Crowley, G. (2017). Neutral wind and density perturbations in the thermosphere created by gravity waves observed by the TIDDBIT sounder. *Journal of Geophysical Research: Space Physics*, *122*(6), 6652–6678. https://doi.org/10.1002/2016JA023828

Vadas, S. L., & Fritts, D. C. (2001). Gravity wave radiation and mean responses to local body forces in the atmosphere. *Journal of the Atmospheric Sciences*, *58*(16), 2249–2279. https://doi.org/10.1175/1520-0469(2001)058⟨2249:GWRAMR⟩2.0.CO;2

Vadas, S. L., & Fritts, D. C. (2004). Thermospheric responses to gravity waves arising from mesoscale convective complexes. *Journal of Atmospheric and Solar-Terrestrial Physics*, *66*(6–9), 781–804. https://doi.org/10.1016/j.jastp.2004.01.025

Vadas, S. L., & Fritts, D. C. (2005). Thermospheric responses to gravity waves: Influences of increasing viscosity and thermal diffusivity. *Journal of Geophysical Research*, *110*(D15), D15103. https://doi.org/10.1029/2004JD005574

Vadas, S. L., & Fritts, D. C. (2006). Influence of solar variability on gravity wave structure and dissipation in the thermosphere from tropospheric convection. *Journal of Geophysical Research*, *111*(A10), A10S12. https://doi.org/10.1029/2005JA011510

Vadas, S. L., & Fritts, D. C. (2009). Reconstruction of the gravity wave field from convective plumes via ray tracing. *Annals of Geophysics*, *27*(1), 147–177. https://doi.org/10.5194/angeo-27-147-2009

Vadas, S. L., Fritts, D. C., & Alexender, M. J. (2003). Mechanism for the generation of secondary waves in wave breaking regions. *Journal of the Atmospheric Sciences*, *60*, 194214. https://doi.org/10.1175/1520-0469(2003)060⟨0194:MFTGOS⟩2.0.CO;2

Vadas, S. L., & Nicolls, M. J. (2009). Temporal evolution of neutral, thermospheric winds and plasma response using PFISR measurements of gravity waves. *Journal of Atmospheric and Solar-Terrestrial Physics*, *71*(6–7), 740–770. https://doi.org/10.1016/j.jastp.2009.01.011

Vadas, S. L., Xu, S., Yue, J., Bossert, K., Becker, E., & Baumgarten, G. (2019). Characteristics of the quiet-time hot spot gravity waves observed by GOCE over the southern Andes on 5 July 2010. *Journal of Geophysical Research: Space Physics*, *124*(8), 7034–7061. https://doi.org/10.1029/2019JA026693

Vadas, S. L., Yue, J., & Nakamura, T. (2012). Mesospheric concentric gravity waves generated by multiple convective storms over the North American great plain. *Journal of Geophysical Research*, *117*(D7), D07113. https://doi.org/10.1029/2011JD017025

Vadas, S. L., Yue, J., She, C.-Y., Stamus, P. A., & Liu, A. Z. (2009). A model study of the effects of winds on concentric rings of gravity waves from a convective plume near Fort Collins on 11 may 2004. *Journal of Geophysical Research*, *114*(D6), D06103. https://doi.org/10.1029/2008JD010753

Wang, M., Ding, F., Wan, W., Ning, B., & Zhao, B. (2007). Monitoring global traveling ionospheric disturbances using the worldwide GPS network during the October 2003 storms. *Earth Planets and Space*, *59*(5), 407–419. https://doi.org/10.1186/BF03352702

Wang, Y., Zhang, L., Zhang, Y., & Guan, J. (2019). Effects of tropospheric vertical wind shear on gravity waves generated by tropical cyclones. *Geophysical Research Letters*, *46*(8), 4523–4530. https://doi.org/10.1029/2019GL082085

Xu, J., Li, Q., Yue, J., Hoffmann, L., Straka, W. C., Wang, C., et al. (2015). Concentric gravity waves over northern China observed by an airglow imager network and satellites. *Journal of Geophysical Research: Atmospheres*, *120*(21), 11058–11078. https://doi.org/10.1002/2015JD023786